



OPEN

On the measurement of skeletal muscle anisotropic permittivity property with a single cross-shaped needle insertion

Hyeuknam Kwon^{1✉}, Hyoung Churl Park², Albert Cheto Barrera³, Seward B. Rutkove⁴ & Benjamin Sanchez^{3✉}

Application of minimally invasive methods to enable the measurement of tissue permittivity in the neuromuscular clinic remain elusive. This paper provides a theoretical and modeling study on the measurement of the permittivity of two-dimensional anisotropic tissues such as skeletal muscle with a multi-electrode cross-shaped needle. For this, we design a novel cross-shaped needle with multiple-electrodes and analyse apparent impedance corresponding to the measured impedance. In addition, we propose three methods of estimate anisotropic muscle permittivity. Compared to existing electrical impedance-based needle methods that we have developed, the new needle design and numerical methods associated enable estimating *in vivo* muscle permittivity values with only a single needle insertion. Being able to measure muscle permittivity directly with a single needle insertion could open up an entirely new area of research with direct clinical application, including using these values to assist in neuromuscular diagnosis and to assess subtle effects of therapeutic intervention on muscle health.

Understanding the basic characteristics of electrical current flow through muscle is needed for improving the accuracy of existing analytical techniques, such as needle electromyography, as well as developing new diagnostic tools for neuromuscular disorder (NMD) assessment. For example, volume conduction theory explains that high frequency electrical events generated during myofiber depolarization are visible only when the recording electrodes are in close proximity to the myofiber source, whereas low frequency events attenuate less and can propagate through the extracellular space over a long distance^{1–3}. This low-pass filtering characteristics affects the morphology (i.e., in amplitude and latency) of extracellular local field potentials in muscle tissue. These changes are likely the result of complex interactions of many NMD-related tissue alterations affecting the extracellular conducting medium (e.g., myofiber atrophy and fatty infiltration in dystrophic muscle)^{4,5}. Although these underlying alterations directly affect the microenvironment's passive, linear permittivity property (i.e., conductivity and relative permittivity) as well as their spatial dependence and are a main determinant of the frequency-filtering properties of electrical potential distribution within diseased muscle, evaluation of these changes using standard needle electromyography (EMG) is not possible⁶.

Methods for measuring the muscle permittivity have limitations. Magnetic resonance electrical properties (MR-EP) imaging can provide noninvasive imaging of tissue permittivity; however, it has been mainly applied to the central nervous system⁷. Also, the technique requires subjects to go to a specialized facility, it cannot be used in children without sedation, subjects must lie flat—a major problem in people with respiratory compromise, a common situation in patients with NMD—, it can put subjects with implanted pacemakers at risk, it is very expensive to perform, and the test is slow, typically taking 45 min or longer to perform. Perhaps most importantly, MR-EP imaging can only assess tissue permittivity at a single frequency determined by the strength of the magnetic field (typically >100 MHz) and thus these electrical properties have limited value to aid in the interpretation of EMG data, which is typically in the Hz to kHz frequency range.

The gold standard electrical impedance-based method for measuring muscle permittivity is muscle biopsy^{8–10}, in which a sample of freshly excised muscle is studied. However, due to the invasiveness^{11,12}, researchers have

¹Division of Software, Yonsei University, Wonju, Republic of Korea. ²Department of Mathematics, Yonsei University, Wonju, Republic of Korea. ³Department of Electrical and Computer Engineering, University of Utah, Salt Lake City, UT 84112, USA. ⁴Department of Neurology, Beth Israel Deaconess Medical Center, Harvard Medical School, Boston, MA 02215, USA. ✉email: hyeuknamkwon@yonsei.ac.kr; benjamin.sanchez@utah.edu

Symbol	Unit	Description
θ	Radian	Needle azimuthal angle, set to be 0 in this paper
φ	Radian	Needle polar angle, set to be 0 in this paper
ϕ	Radian	Needle rotation angle, set to be positive number in this paper
a	m	Distance between the first and second rows of the electrode array (= third and fourth rows)
b	m	Distance between the second and third rows of the electrode array
s	m	Distance between two columns of electrode array
κ_L and κ_T	Ω m	Longitudinal and transverse impedivity
$\bar{\kappa}$	Ω m	Geometric mean of the impedivity, defined as $\bar{\kappa} := \sqrt{\kappa_L \kappa_T}$
ρ_L and ρ_T	Ω m	Longitudinal and transverse resistivity
τ_L and τ_T	Ω m	Longitudinal and transverse reactivity
α^2	Dimensionless	Anisotropy ratio of the muscle, defined as ρ_L / ρ_T
$K_{\text{half space}}$	Dimensionless	Domain factor of the half space, that is 2π
\hat{K}_i and \hat{K}_i^\perp	Dimensionless	Domain factor of the needle for $i = 1, 2, 4, 6, 17$
Z_i and \hat{Z}_i	Ω	Measured and simulated apparent impedance for $i = 1, 2, 4, 6, 17$

Table 1. Symbols and parameters used in this study.

mainly obtained ex vivo values from laboratory animals. In addition to the limitations in recapitulating the physiopathology of human NMDs, ex vivo animal muscle values differ from in vivo human tissue as these properties change, among others, within animal species^{13–16}, with death^{17,18} and with temperature¹⁹. Another major limitation of biopsy is the inability to follow the natural progression or remission of NMDs over time because of sampling limitations.

To allow the measurement of in vivo muscle permittivity values^{20,21}, we developed needle electrical impedance myography (EIM) and associated methods^{22,23}. While promising, these methods required multiple simultaneous needle insertions. Thus, it became clear that further research was still needed to facilitate clinical adoption by minimizing patient discomfort to only a single needle insertion²⁴. Here, we present an innovative cross-shaped EIM needle and associated (iterative) inverse methods for estimating in vivo muscle permittivity with only a single needle insertion.

The rest of the text consists of three sections; “Methods”, “Results”, and “Discussion”. In the “Methods” section, we define needle model and muscle domain model and derive the equation of apparent electrical impedance of using the needle in the muscle model (in the subsection “Forward problem”). Based on the apparent electrical impedance equation, three methods for estimating the anisotropic permittivity properties of muscles are introduced in the inverse methods subsection (in the subsection “inverse methods”). Finally, this section describes the setting up of numerical experiments to verify these methods (in the subsection “Numerical simulations”). The results section provides numerical simulation results applying the three methods. Numerical simulations are designed to validate Convergence, Sensitivity, and Robustness. In addition, the results of estimating the electrical properties of the anisotropic muscle are also presented. The final section of the paper is the “Discussion” section.

Methods

Table 1 summarizes the relevant nomenclature, including symbols and parameters, that is used throughout the manuscript.

Forward problem. Needle and muscle domain models. We propose a cross-type ‘+’ needle shown in Fig. 1a containing 64 point-like electrodes distributed in the eight faces of the needle (Fig. 1b), each face referred as to $[F_1 F_2]$ where F_1 and F_2 denote the face’s cardinal point and orientation respectively, i.e., $F_1, F_2 \in \{N, S, W, E\}$, so that when $F_1 \in \{N, S\}$ then $F_2 \in \{E, W\}$ and when $F_1 \in \{E, W\}$ then $F_2 \in \{N, S\}$ as in Fig. 1b. Each face has eight electrodes ε_{ik} distributed in a four rows \times two columns, where $i = 1, 2, 3, 4$ is the row index and $k = 1, 2$ is the column index. The distance a (m) is defined between the outermost electrodes and the nearest electrodes, i.e., ε_{1k} to ε_{2k} and ε_{3k} to ε_{4k} , while the distance b (m) is defined between the inner electrodes ε_{2k} to ε_{3k} . The distance from both the needle tip and the needle’s upper edge to the nearest electrodes ε_{1k} and ε_{4k} is a_0 (m), respectively. The distance between ε_{i1} and ε_{i2} is s (m). Finally, both distances from ε_{i1} to the needle’s major axis and from ε_{i2} to the lateral edge is c (m). We then assume that the four arms of the needle define four semi-infinite subdomains in Fig. 1c, namely $\Omega_1 = \{x > 0, y > 0, z \in \mathbb{R}\}$, $\Omega_2 = \{x < 0, y > 0, z \in \mathbb{R}\}$, $\Omega_3 = \{x < 0, y < 0, z \in \mathbb{R}\}$ and $\Omega_4 = \{x > 0, y < 0, z \in \mathbb{R}\}$. In other words, the needle arms’ thickness is considered negligible.

The needle is inserted through the skin and subcutaneous fat tissues into the muscle as shown in Figure 2. We define the x, y -axes transverse to the longitudinal direction determined by the muscle fibers in the z -axis. They are defined to form the canonical basis in \mathbb{R}^3 and for the needle’s major axis to be located in the first quadrant of the yz plane. We use spherical coordinates to define the position of the needle’s major axis, with the origin of coordinates defined by convention located in the needle’s tip. The polar angle is defined by $\varphi \in [0, \pi/2]$. By definition of the axes the azimuthal angle θ is always 0. The rotation angle $\phi \in [0, 2\pi)$ defines the needle’s rotation angle with respect to its major axis.

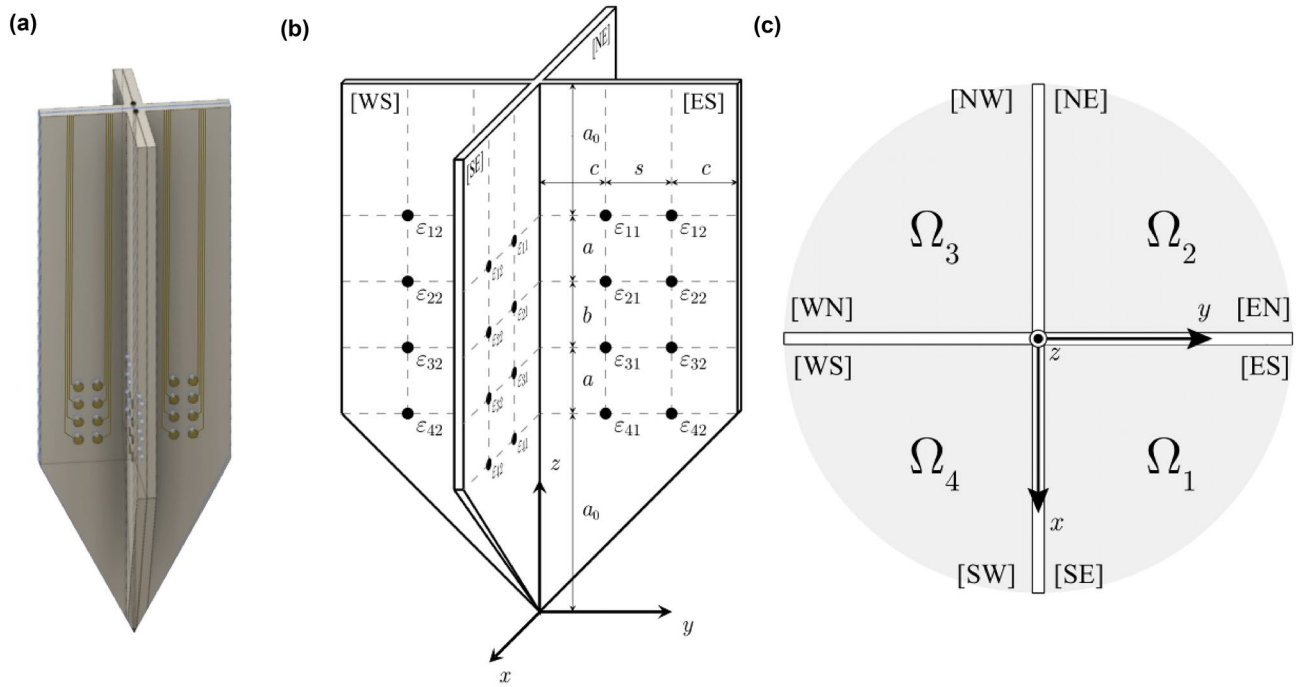


Figure 1. (a) Schematic representation of the needle. (b) Needle's geometry (not to scale). (c) Needle's top view.

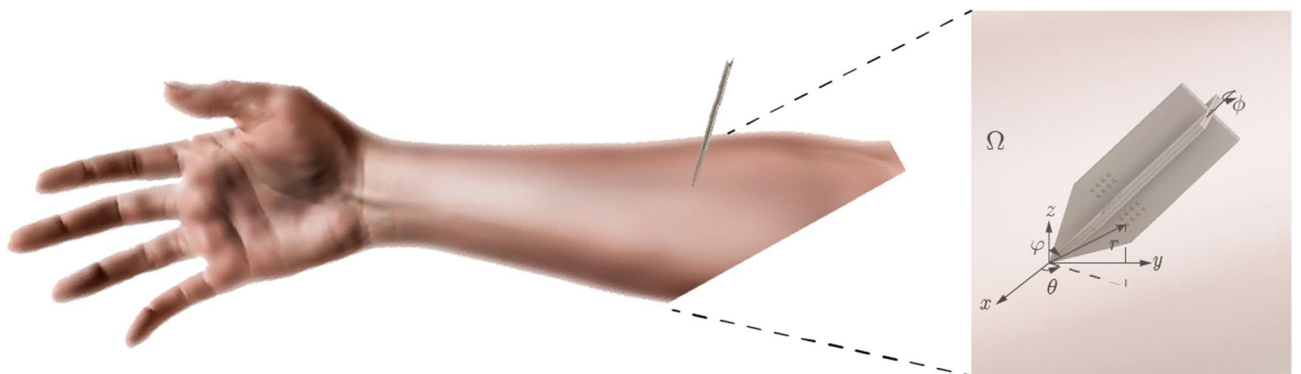


Figure 2. Insertion of the needle to the skeletal muscle and inlet representing a model abstraction of an arbitrary geometrical arrangement of muscle domain Ω and needle to illustrate the spherical coordinate system used.

As a convention, when $\theta = \phi = 0$, then the needle's major axis is aligned with respect to the z -axis and the [ES] face is the yz plane. Finally, we define when $\phi = \pi/2$ then $\phi \in [0, \pi)$.

Electrodes' position in spherical coordinates. Unless otherwise noted, henceforth we restrict ourselves to study an impedance measurement with the electrodes in the face [ES]. The position $\mathbf{P}_{ik} := (x_{ik}, y_{ik}, z_{ik}) \in \mathbb{R}^3$ of electrode ϵ_{ik} by default, i.e., $\phi = \phi = \theta = 0$, is

$$\begin{aligned} \mathbf{P}_{11} &= (0, c, 2a + b + a_0) & \mathbf{P}_{12} &= (0, c + s, 2a + b + a_0) \\ \mathbf{P}_{21} &= (0, c, a + b + a_0) & \mathbf{P}_{22} &= (0, c + s, a + b + a_0) \\ \mathbf{P}_{31} &= (0, c, a + a_0) & \mathbf{P}_{32} &= (0, c + s, a + a_0) \\ \mathbf{P}_{41} &= (0, c, a_0) & \mathbf{P}_{42} &= (0, c + s, a_0) \end{aligned} \quad (1)$$

as we see in Fig. 1b. For notational simplicity, we denote the electrode position by $(0, y_{ik}, z_{ik}) := \mathbf{P}_{ik}$ for $i = 1, 2, 3, 4$ and $k = 1, 2$. To describe the general position of an electrode we use three dimensional rotation matrices. The rotation matrices along x -, y -, and z - axes with an angle δ using right-hand rule are

$$R_x(\delta) := \begin{bmatrix} 1 & 0 & 0 \\ 0 & \cos \delta & -\sin \delta \\ 0 & \sin \delta & \cos \delta \end{bmatrix}, \quad R_y(\delta) := \begin{bmatrix} \cos \delta & 0 & -\sin \delta \\ 0 & 1 & 0 \\ \sin \delta & 0 & \cos \delta \end{bmatrix} \quad \text{and} \quad R_z(\delta) := \begin{bmatrix} \cos \delta & -\sin \delta & 0 \\ \sin \delta & \cos \delta & 0 \\ 0 & 0 & 1 \end{bmatrix}. \quad (2)$$

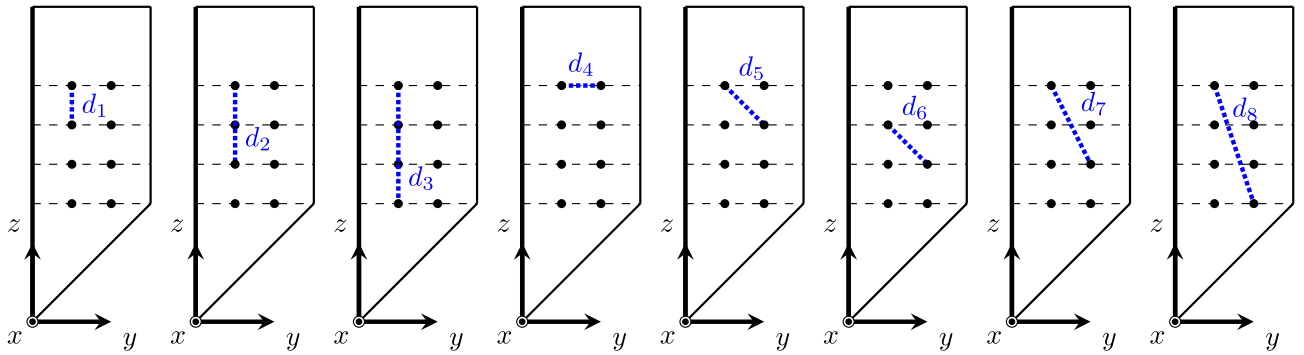


Figure 3. The eight different distances between two same face electrodes. Face [ES] in default side shown.

The rotated electrode position $\mathbf{Q}_{ik} \in \mathbb{R}^3$ is defined as $\mathbf{Q}_{ik} := R_x(-\varphi)R_z(\phi)\mathbf{P}_{ik}$, that is

$$\mathbf{Q}_{ik} = \begin{bmatrix} -y_{ik} \sin \phi \\ y_{ik} \cos \phi \cos \varphi + z_{ik} \sin \varphi \\ -y_{ik} \cos \phi \sin \varphi + z_{ik} \cos \varphi \end{bmatrix} =: \begin{bmatrix} \mathbf{Q}_{ik}(x) \\ \mathbf{Q}_{ik}(y) \\ \mathbf{Q}_{ik}(z) \end{bmatrix}. \tag{3}$$

If we want to describe the position of an electrode in another face it is equivalent to consider the electrode to be in the [ES] face changing the angle ϕ for $\phi + t\pi/2$ with $t \in \mathbb{Z}$.

Apparent electrical impedance. We define the impedivity $\kappa (\Omega \text{ m}) \in \mathbb{C}$ as

$$\kappa := \rho + j\tau = \frac{\sigma}{\sigma^2 + (\omega\epsilon_0\epsilon_r)^2} - j \frac{\omega\epsilon_0\epsilon_r}{\sigma^2 + (\omega\epsilon_0\epsilon_r)^2}, \tag{4}$$

where ρ and τ are the resistivity and reactivity, respectively, $j^2 = -1$ is the imaginary unit (dimensionless), σ is the conductivity (S m^{-1}), ω is the angular frequency (rad s^{-1}), ϵ_0 is the vacuum permittivity (F m^{-1}) and ϵ_r is the relative permittivity (dimensionless). We note that if $\epsilon_r = 0$, then $\kappa = \rho = 1/\sigma$.

Let $\alpha^2 := \frac{\rho_L}{\rho_T} := \frac{\tau_L}{\tau_T} \leq 1$ be the anisotropy ratio (dimensionless), where the subscripts {T,L} denote the transverse x, z -axes and longitudinal y -axis directions. Following Plonsey and Heppner³³ and Kwon et al.²⁰ work, the potential $V (V) \in \mathbb{C}$ created by a point current electrode in an homogeneous infinite anisotropic material is

$$V := \frac{\bar{\kappa} I}{K \|\mathbf{r}_\alpha - \mathbf{r}_0\|_2} = \frac{\bar{\kappa} I}{K \sqrt{(x - x_0)^2 + \alpha^2(y - y_0)^2 + (z - z_0)^2}}, \tag{5}$$

where $\bar{\kappa} := \sqrt{\kappa_L \kappa_T}$ is the geometric mean of the longitudinal and transverse impedivities, I is the current (A), $K := 2\pi$ is a domain factor (dimensionless) from assuming that the needle face delimits the muscle in a semi-infinite region³⁴. The operator $\|\cdot\|_2$ is the L_2 norm, $\mathbf{r}_0 := (x_0, \alpha y_0, z_0)$ and $\mathbf{r}_\alpha := (x, \alpha y, z)$ are the apparent position of current and voltage electrodes, respectively.

For notational convenience, we define the apparent distance d_α m between two electrodes ($\mathbf{Q}_{ik}, \mathbf{Q}_{nl}$) as

$$d_\alpha(\mathbf{Q}_{ik}, \mathbf{Q}_{nl}) := \sqrt{(\mathbf{Q}_{ik}(x) - \mathbf{Q}_{nl}(x))^2 + \alpha^2(\mathbf{Q}_{ik}(y) - \mathbf{Q}_{nl}(y))^2 + (\mathbf{Q}_{ik}(z) - \mathbf{Q}_{nl}(z))^2}. \tag{6}$$

Using the expression above and the position of electrodes in Eq. (3) we obtain

$$d_\alpha(\mathbf{Q}_{ik}, \mathbf{Q}_{nl}) = \sqrt{(y_{ik} - y_{nl})^2 A + (z_{ik} - z_{nl})^2 B + (y_{ik} - y_{nl})(z_{ik} - z_{nl}) C}, \tag{7}$$

where

$$\begin{aligned} A &:= \sin^2 \phi + \cos^2 \phi (\alpha^2 \cos^2 \varphi + \sin^2 \varphi), \\ B &:= 1, \\ C &:= 2(\alpha^2 - 1) \cos \phi \sin \varphi \cos \varphi = (\alpha^2 - 1) \cos \phi \sin 2\varphi, \end{aligned} \tag{8}$$

are variables that only depend on the needle orientation and the anisotropy ratio. As expected, when $\alpha^2 = 1$ (i.e., isotropic muscle) the dependence of d_α with the orientation of the needle is lost. If we choose two electrodes on the same face, there are eight different distances considering the electrodes' distribution (see Fig. 3). We define them as $d_{1,\dots,8}$

$$\begin{aligned}
 d_1 &:= d_\alpha(\mathbf{Q}_{in}, \mathbf{Q}_{(i+1)n}) = a\sqrt{B}, i \in \{1, 3\}, n \in \{1, 2\}, \\
 d_2 &:= d_\alpha(\mathbf{Q}_{in}, \mathbf{Q}_{(i+2)n}) = (a + b)\sqrt{B}, i \in \{1, 2\}, n \in \{1, 2\}, \\
 d_3 &:= d_\alpha(\mathbf{Q}_{1n}, \mathbf{Q}_{4n}) = (2a + b)\sqrt{B}, n \in \{1, 2\}, \\
 d_4 &:= d_\alpha(\mathbf{Q}_{i1}, \mathbf{Q}_{i2}) = s\sqrt{A}, i \in \{1, 2, 3, 4\}, \\
 d_5 &:= d_\alpha(\mathbf{Q}_{in}, \mathbf{Q}_{(i+1)k}) = \sqrt{s^2A + a^2B + saC}, i \in \{1, 3\}, \{n, k\} = \{1, 2\}, \\
 d_6 &:= d_\alpha(\mathbf{Q}_{2n}, \mathbf{Q}_{3k}) = \sqrt{s^2A + b^2B + sbC}, \{n, k\} = \{1, 2\}, \\
 d_7 &:= d_\alpha(\mathbf{Q}_{in}, \mathbf{Q}_{(i+2)k}) = \sqrt{s^2A + (a + b)^2B + s(a + b)C}, i \in \{1, 2\}, \{n, k\} = \{1, 2\}, \\
 d_8 &:= d_\alpha(\mathbf{Q}_{1n}, \mathbf{Q}_{4k}) = \sqrt{s^2A + (2a + b)^2B + s(2a + b)C}, \{n, k\} = \{1, 2\}.
 \end{aligned}
 \tag{9}$$

To perform an impedance measurement, we need four electrodes being positive and negative current and voltage electrodes which are denoted by $\varepsilon_{I^+}, \varepsilon_{I^-}, \varepsilon_{V^+}$ and ε_{V^-} , respectively. Their positions are denoted by $\mathbf{Q}_{I^+}, \mathbf{Q}_{I^-}, \mathbf{Q}_{V^+}$ and \mathbf{Q}_{V^-} . Considering Eqs. (5) and (7), we can rewrite electrical potential as follows

$$V^{pm} = \frac{\bar{\kappa}I}{Kd_\alpha(\mathbf{Q}_{V^p}, \mathbf{Q}_{I^m})}, \tag{10}$$

where $p, m \in \{+, -\}$ and V^{pm} is the electric potential measured at ε_{V^p} when current I generated at ε_{I^m} . Finally, we define the impedance as

$$Z := \frac{V^{++} - V^{+-} - V^{-+} + V^{--}}{I} \tag{11}$$

To measure the impedance using the four electrode method, we will have to measure the distance between two electrode roles instead of two electrodes. Therefore, $d_\alpha(\cdot, \cdot)$ in Eq. (10) is presented like so. If we choose four electrodes on the same face for an impedance measurement, i.e., $\varepsilon_{I^+}, \varepsilon_{I^-}, \varepsilon_{V^+}$ and ε_{V^-} , there are $\binom{8}{4} \cdot 4! = 1680$ possibilities. Most of the configurations give redundant information so we restrict ourselves to nineteen configurations (see Fig. 4). Configurations 1 to 16 in Fig. 4 verify $\{\varepsilon_{11}, \varepsilon_{12}\} \in \varepsilon_{I^+}, \{\varepsilon_{41}, \varepsilon_{42}\} \in \varepsilon_{I^-}, \{\varepsilon_{21}, \varepsilon_{22}\} \in \varepsilon_{V^+}$ and $\{\varepsilon_{31}, \varepsilon_{32}\} \in \varepsilon_{V^-}$. Configurations 17 to 19 are rectangular configurations. The expressions of the impedance for each configuration in Fig. 4 are presented in Table 2. Note that two configurations that have the sets $\{d_\alpha(\mathbf{Q}_{V^+}, \mathbf{Q}_{I^+}), d_\alpha(\mathbf{Q}_{V^-}, \mathbf{Q}_{I^-})\}$ and $\{d_\alpha(\mathbf{Q}_{V^+}, \mathbf{Q}_{I^-}), d_\alpha(\mathbf{Q}_{V^-}, \mathbf{Q}_{I^+})\}$ equal give the same impedance value as shown in Table 2.

In this paper, we choose to use five different current-voltage configurations (1, 2, 4, 6, 17 in Fig. 4) to measure apparent impedance Z . Using Eqs. (5) and (11), the impedance values are

$$Z_1 = \frac{\bar{\kappa}}{K} \frac{2b}{a(a + b)} \tag{12}$$

$$Z_2 = \frac{\bar{\kappa}}{K} \left(\frac{1}{a\sqrt{B}} - \frac{1}{\sqrt{s^2A + (a + b)^2B + s(a + b)C}} - \frac{1}{(a + b)\sqrt{B}} + \frac{1}{\sqrt{s^2A + a^2B + saC}} \right) \tag{13}$$

$$Z_4 = \frac{2\bar{\kappa}}{K} \frac{[s^2A + (a + b)^2 + (a + b)sC]\sqrt{B} - aB\sqrt{s^2A + (a + b)^2B + (a + b)sC}}{aB[s^2A + (a + b)^2B + (a + b)sC]} \tag{14}$$

$$Z_6 = \frac{2\bar{\kappa}}{K} \frac{(a + b)B\sqrt{s^2A + a^2B + asC} - \sqrt{B}(s^2A + a^2B + asC)}{(s^2A + a^2B + asC)(a + b)B} \tag{15}$$

$$Z_{17} = \frac{2\bar{\kappa}}{K} \frac{a\sqrt{B} - s\sqrt{A}}{as\sqrt{AB}} \tag{16}$$

Here, $A, B,$ and C are defined in Eq. (8).

Of note, Z_i with $i = \{1, 2, 4, 6, 17\}$ are inversely proportional to the *unknown* geometric factor K (dimensionless), the latter dependent on the electrode size and the inter-electrode distances. We propose an empirical needle geometric factor of the needle \hat{K}_i and \hat{K}_i^\perp as

$$\hat{K}_i(\alpha^2, \phi) = K_{\text{half space}} \frac{Z_i(\alpha^2, \phi)}{\hat{Z}_i(\alpha^2, \phi)} \quad \text{and} \quad \hat{K}_i^\perp(\alpha^2, \phi) = \hat{K}_i(\alpha^2, \phi - \pi/2) \tag{17}$$

for given anisotropy ratio α^2 and needle rotation angle ϕ , where $K_{\text{half space}}$ is 2π , $Z_i(\alpha^2, \phi)$ is the apparent impedance value derived from Eqs. (12)–(16) with half space domain assumption, and $\hat{Z}_i(\alpha^2, \phi)$ is the simulated apparent impedance value.

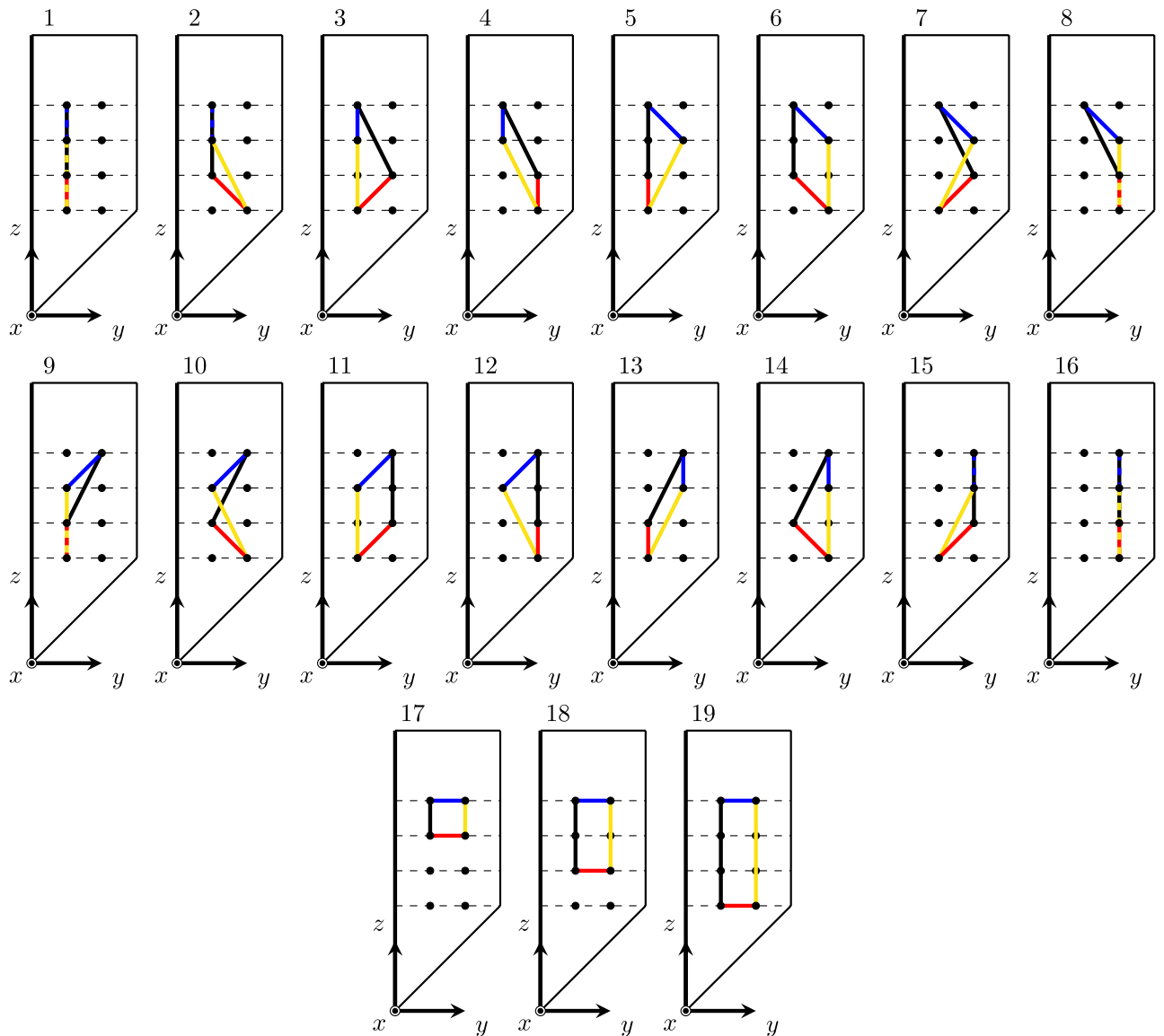


Figure 4. Configurations 1 to 19. In blue, distance for V^{++} . In red, distance for V^{--} . In yellow, distance for V^{+-} . In black, distance for V^{-+} .

Inverse methods. In this section, we provide three inverse methods to estimate the anisotropic permittivity properties of muscle from apparent impedance values measured using the cross-shaped needle electrodes. Methods are presented in increasing complexity:

1. Method I requires to insert the cross-shaped needle has its major axis is aligned with respect to the z -axis and the [ES] face is the yz -plane as in Fig. 1 b, i.e. $\varphi = \phi = 0$. Method I can be applied using only electrodes on one side, for example electrodes on [ES].
2. The needle of method II rotated the needle of method I about the z -axis by known angle ϕ , i.e. $\varphi = 0$ and ϕ don't need to be zero. Method II can be applied using only electrodes on one side, for example electrodes on [ES].
3. The needle position of method II is same as that of method III, but method III does not require to know the needle rotation angle ϕ . Method III requires the use of electrodes on two facing sides, for example electrodes on [ES] and [SE].

The key idea of the iteration process is to update the needle geometric factor K in Eqs. (12)–(16). We use \hat{K}_i in Eq. (17) to estimate K . To do that, we built a dataset of \hat{K}_i values for each needle electrode model $i = 1, 2, 4, 6, 17$ while changing muscle anisotropy and needle rotation angle in numerical simulations. Indeed, in order to make a dataset of \hat{K}_i with fixed needle electrode model, we perform several numerical simulations with various $\alpha^2 \in (0, 1]$ and $\phi \in [0, \pi/2]$.

Configurations	Impedance	Q subscript			
		I ⁺	V ⁺	V ⁻	I ⁻
1	$Z_1 = \frac{2\bar{\kappa}}{K} \left(\frac{1}{d_1} - \frac{1}{d_2} \right)$	11	21	31	41
2	$Z_2 = \frac{\bar{\kappa}}{K} \left(\frac{1}{d_1} - \frac{1}{d_7} - \frac{1}{d_2} + \frac{1}{d_5} \right)$	11	21	31	42
3	$Z_3 = Z_2$	11	21	32	41
4	$Z_4 = \frac{2\bar{\kappa}}{K} \left(\frac{1}{d_1} - \frac{1}{d_7} \right)$	11	21	32	42
5	$Z_5 = Z_2$	11	22	31	41
6	$Z_6 = \frac{2\bar{\kappa}}{K} \left(\frac{1}{d_5} - \frac{1}{d_2} \right)$	11	22	31	42
7	$Z_7 = \frac{2\bar{\kappa}}{K} \left(\frac{1}{d_5} - \frac{1}{d_7} \right)$	11	22	32	41
8	$Z_8 = Z_2$	11	22	32	42
9	$Z_9 = Z_2$	12	21	31	41
10	$Z_{10} = Z_7$	12	21	31	42
11	$Z_{11} = Z_6$	12	21	32	41
12	$Z_{12} = Z_2$	12	21	32	42
13	$Z_{13} = Z_4$	12	22	31	41
14	$Z_{14} = Z_2$	12	22	31	42
15	$Z_{15} = Z_2$	12	22	32	41
16	$Z_{16} = Z_1$	12	22	32	42
17	$Z_{17} = \frac{2\bar{\kappa}}{K} \left(\frac{1}{d_4} - \frac{1}{d_1} \right)$	11	12	21	22
18	$Z_{18} = \frac{2\bar{\kappa}}{K} \left(\frac{1}{d_4} - \frac{1}{d_2} \right)$	11	12	31	32
19	$Z_{19} = \frac{2\bar{\kappa}}{K} \left(\frac{1}{d_4} - \frac{1}{d_3} \right)$	11	12	41	42

Table 2. Table of the nineteen configurations in Fig. 4 with its impedance equation (11) and the electrode involved for each role.

Inverse Method I: Z_1 and Z_i are measured in $\theta = 0$ (or $\pi/2$), $\phi = 0$, $\varphi = 0$ for $i \in \{2, 4, 6, 17\}$.

Assumption 1. The major muscle fibers orientation is known and the needle axis is aligned on the z -axis (i.e., the needle is inserted perpendicularly to the muscle fibers).

Method I uses four electrodes on a plane parallel to the direction of the muscle fibre (e.g. [ES] plane in Fig. 1). On the selected plane, we measure two impedances Z_1 and Z_i for $i = 2, 4, 6, 17$ as in Fig. 4. The measured Z_1 is used to compute $\bar{\kappa}$ and measured Z_i is used to compute α^2 . The flowchart can be seen in Fig. 5.

Estimation of $\bar{\kappa}$. We estimate $\bar{\kappa}$ as a convergence value of κ_n , i.e. $\bar{\kappa} := \lim_{n \rightarrow \infty} \kappa_n$, and define κ_n as

$$\kappa_n = \frac{a(a+b)Z_1K_1(\alpha_{n,i}^2, 0)}{2b} \tag{18}$$

where $\alpha_{n,i}^2$ is estimated anisotropy ratio at n -th iteration for $i = 2, 4, 6, 17$ which indicates used impedance value.

Estimation of α^2 . We estimate α^2 as a convergence value of $\alpha_{n,i}^2$, i.e. $\alpha^2 := \lim_{n \rightarrow \infty} \alpha_{n,i}^2$ for $i = 2, 4, 6, 17$. Note here that n is for iteration number and i is for used impedance number. We propose here four methods to estimate $\alpha_{n,i}^2$ of using Z_i for $i = 2, 4, 6, 17$.

- Using Z_2 : $\alpha_{n,2}^2$ is the solution of below equation

$$Q^4x^4 - 4(Q^2 + 2Q^4R)x^3 - 6(Q^2R + Q^4R^2)x^2 - 2Q^2R^2 + R^2 = 0 \tag{19}$$

where $Q := \frac{Z_2\bar{\kappa}_2(\alpha_{n-1,2}^2, 0)}{\kappa_{n-1}} - \frac{1}{a} + \frac{1}{a+b}$ and $R := 2ab + b^2$.

- Using Z_4 :

$$\alpha_{n,4}^2 = \frac{Q - (a+b)^2}{s^2} \tag{20}$$

where $Q := \left(\frac{2a\kappa_{n-1}}{aZ_4\bar{\kappa}_4(\alpha_{n-1,4}^2, 0) - 2\kappa_{n-1}} \right)^2$.

- Using Z_6 :

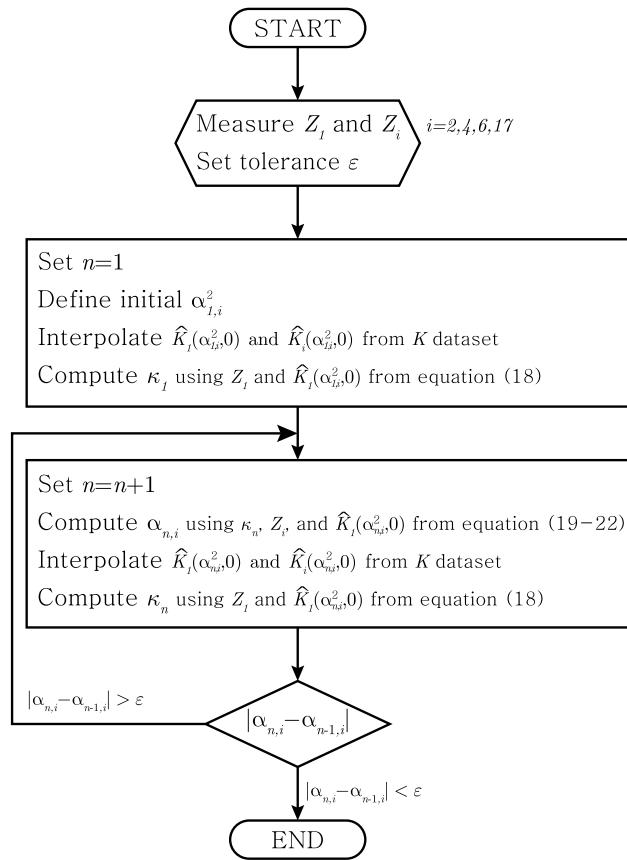


Figure 5. Iteration scheme of the method I.

$$\alpha_{n,6}^2 = \frac{Q - a^2}{s^2} \tag{21}$$

when $Q := \left(\frac{2a(a+b)\kappa_{n-1}}{(a+b)Z_6\widehat{K}_6(\alpha_{n-1,6}^2, 0) + 2\kappa_{n-1}} \right)^2$

- Using Z_{17} :

$$\alpha_{n,17}^2 = \left(\frac{2a\kappa_{n-1}}{asZ_{17}\widehat{K}_{17}(\alpha_{n-1,17}^2, 0) + 2\kappa_{n-1}} \right)^2 \tag{22}$$

Inverse Method II: Z_1 and Z_i are measured in $\theta = 0, \phi = 0$ for $i \in \{2, 4, 6, 17\}$.

Assumption 1. Same as method I

Assumption 2. Known $\phi \neq 0$

Method II uses four electrodes on a plane with an angle ϕ to the direction of the muscle fibre. On the selected plane, we measure two impedances Z_1 and Z_i for $i = 2, 4, 6, 17$ as in Fig. 4. The measured Z_1 is used to compute $\bar{\kappa}$ and measured Z_i is used to compute α^2 . The flowchart can be seen in Fig. 6.

Estimation of $\bar{\kappa}$. We estimate $\bar{\kappa}$ as a convergence value of κ_n below

$$\kappa_n = \frac{a(a+b)Z_1\widehat{K}_1(\alpha_{n,i}^2, \phi)}{2b} \tag{23}$$

for $i = 2, 4, 6, 17$.

Estimation of α^2 . We estimate α^2 as a convergence value of $\alpha_{n,i}^2$ for $i = 2, 4, 6, 17$ which is defined as

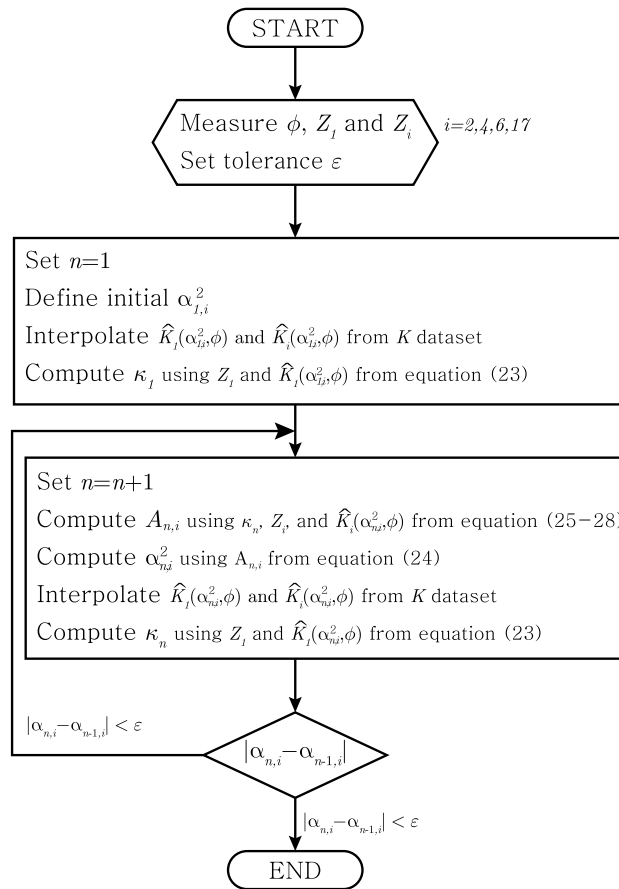


Figure 6. Iteration scheme of the method II.

$$\alpha_{n,i}^2 = \frac{A_{n,i} - \sin^2 \phi}{\cos^2 \phi} \tag{24}$$

Here, $A_{n,i}$ are defined as below ($i = 2, 4, 6, 17$):

- Using Z_2 , $A_{n,2}$ is a solution of the following 4th degree polynomial.

$$P^4 x^4 + (-4P^2 + 2P^4 R)x^3 + (-6P^2 R + P^4 R^2)x^2 - 2P^2 R^2 + R^2 \tag{25}$$

- where $R := 2ab + b^2$ and $P := \frac{Z_2 \hat{K}_2(\alpha_{n-1,2}^2, \phi)}{\kappa_{n-1}} - \frac{1}{a} + \frac{1}{a+b}$.
- Using Z_4 ,

$$A_{n,4} = \frac{Q_{n-1} - (a + b)^2}{s^2} \tag{26}$$

- where $Q_{n-1} := \left(\frac{2a\kappa_{n-1}}{aZ_4 \hat{K}_4(\alpha_{n-1,4}^2, \phi) - 2\kappa_{n-1}} \right)^2$
- Using Z_6 ,

$$A_{n,6} = \frac{Q_{n-1} - a^2}{s^2} \tag{27}$$

- where $Q_{n-1} := \left(\frac{2a(a+b)\kappa_{n-1}}{(a+b)Z_6 \hat{K}_6(\alpha_{n-1,6}^2, \phi) + 2\kappa_{n-1}} \right)^2$
- Using Z_{17} ,

$$A_{n,17} = \left(\frac{2\kappa_{n-1}}{asZ_{17} \hat{K}_{17}(\alpha_{n-1,17}^2, \phi) + 2\kappa_{n-1}} \right)^2 \tag{28}$$

Inverse Method III: $Z_1, Z_1^\perp, Z_i,$ and Z_i^\perp are measured in $\theta = 0, \phi = 0$ for $i \in \{2, 4, 6, 17\}$.

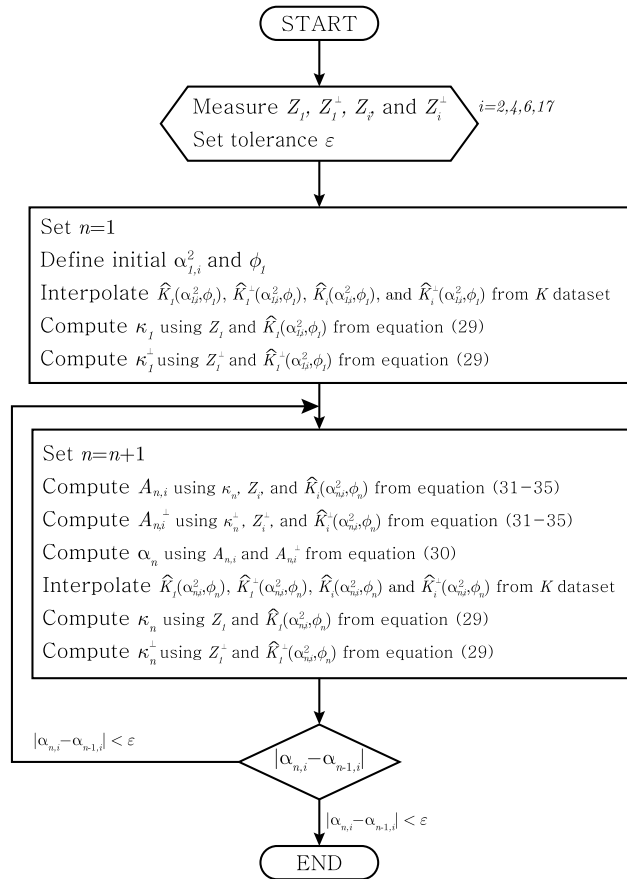


Figure 7. Iteration scheme of the method III.

- Assumption 1. Same as method I
- Assumption 2. Unknown $\phi (\neq 0)$

Method III, which does not require to know ϕ , is most practical method in this paper. This method uses four electrodes on one side and two faces perpendicular to each other (e.g. [ES] and [SE] planes in Fig. 1) i.e. eight electrodes total. At first, we compute $\kappa_n (\kappa_n^\perp)$ using the $Z_1 (Z_1^\perp)$ and $K_1 (K_1^\perp)$ in each plane (perpendicular plane). From the $\kappa_n (\kappa_n^\perp)$ and the $Z_i (Z_i^\perp)$ and $K_i (K_i^\perp)$ in each plane, we compute $A (A^\perp)$. Now, α_n is found using A and A^\perp . The loop is made by putting α_n into the K_1 and $K_i (K_1^\perp$ and $K_i^\perp)$. The flowchart can be seen in Fig. 7.

Estimation of $\bar{\kappa}$. We estimate $\bar{\kappa}$ from the convergence value of κ_n and κ_n^\perp . Note here that if the iterative process converges well, then κ_n and κ_n^\perp converges to the same value which is $\bar{\kappa}$.

$$\kappa_n = \frac{Z_1 \widehat{K}_1(\alpha_{n,i}^2, \widehat{\phi}) a(a+b)}{2b} \quad \text{and} \quad \kappa_n^\perp = \frac{Z_1^\perp \widehat{K}_1^\perp(\alpha_{n,i}^2, \widehat{\phi}) a(a+b)}{2b} \tag{29}$$

for $i = 2, 4, 6, 17$.

Estimation of α^2 and ϕ . We estimate α^2 and ϕ as a convergence value of $\alpha_{n,i}^2$ and $\phi_{n,i}$, respectively, as n goes infinity which are defined by

$$\alpha_{n,i}^2 = A_{n,i} + A_{n,i}^\perp - 1 \quad \text{and} \quad \phi_{n,i} = \frac{1}{2} \arccos \left(\frac{2A_{n,i} - 1 - \alpha_{n,i}^2}{\alpha_{n,i}^2 - 1} \right) \tag{30}$$

for $i = 2, 4, 6, 17$. We define $A_{n,i}$ and $A_{n,i}^\perp$ as below:

- Using Z_2 and Z_2^\perp . $A_{n,2}$ and $A_{n,2}^\perp$ can be found by solving the below 4th degree polynomial.

$$P^4 x^4 + (-4P^2 + 2P^4 R)x^3 + (-6P^2 R + P^4 R^2)x^2 - 2P^2 R^2 + R^2 \tag{31}$$

where $R := 2ab + b^2$ and P is defined as below:

$$P := \begin{cases} \frac{Z_2 \widehat{K}_2(\alpha_{n,2}^2, \widehat{\phi})}{\kappa} - \frac{1}{a} + \frac{1}{a+b} & \text{is to find } A_{n,2} \\ \frac{Z_2^\perp \widehat{K}_2^\perp(\alpha_{n,2}^2, \widehat{\phi})}{\kappa} - \frac{1}{a} + \frac{1}{a+b} & \text{is to find } A_{n,2}^\perp \end{cases} \quad (32)$$

- Using Z_4 and Z_4^\perp .

$$A_{n,4} = \frac{Q_{n-1} - (a+b)^2}{s^2}, \quad A_{n,4}^\perp = \frac{Q_{n-1}^\perp - (a+b)^2}{s^2} \quad (33)$$

$$\text{where } Q_{n-1} := \left(\frac{2a\kappa_{n-1}}{aZ_4 \widehat{K}_4(\alpha_{n,4}^2, \widehat{\phi}) - 2\kappa_{n-1}} \right)^2 \text{ and } Q_{n-1}^\perp := \left(\frac{2a\kappa_{n-1}}{aZ_4^\perp \widehat{K}_4^\perp(\alpha_{n,4}^2, \widehat{\phi}) - 2\kappa_{n-1}} \right)^2.$$

- Using Z_6 and Z_6^\perp .

$$A_{n,6} = \frac{Q_{n-1} - a^2}{s^2}, \quad A_{n,6}^\perp = \frac{Q_{n-1}^\perp - a^2}{s^2} \quad (34)$$

$$\text{where } Q_{n-1} := \left(\frac{2a(a+b)\kappa_{n-1}}{(a+b)Z_6 \widehat{K}_6(\alpha_{n,6}^2, \widehat{\phi}) + 2\kappa_{n-1}} \right)^2, \quad Q_{n-1}^\perp := \left(\frac{2a(a+b)\kappa_{n-1}}{(a+b)Z_6^\perp \widehat{K}_6^\perp(\alpha_{n,6}^2, \widehat{\phi}) + 2\kappa_{n-1}} \right)^2$$

- Using Z_{17} and Z_{17}^\perp .

$$A_{n,17} = \left(\frac{2a\kappa_{n-1}}{s(aZ_{17} \widehat{K}_{17}(\alpha_{n,17}^2, \widehat{\phi}) + 2\kappa_{n-1})} \right)^2, \quad (35)$$

$$A_{n,17}^\perp = \left(\frac{2a\kappa_{n-1}}{s(aZ_{17}^\perp \widehat{K}_{17}^\perp(\alpha_{n,17}^2, \widehat{\phi}) + 2\kappa_{n-1})} \right)^2$$

Numerical simulations. The numerical experiments are performed using Comsol (Comsol Multiphysics, Inc., Burlington, MA) and Matlab (The Mathworks, Inc., Natick, MA). In order to simulate needle muscle impedance data, a box in Comsol with $40 \times 40 \times 40$ (cm³) is created. The needle dimensions are length 20 (cm), width 2.15 (cm), and thickness 0.2 (cm). The needle is inserted vertically into the domain, i.e. $\phi = 0, \varphi = 0$ while θ is 0 for method I and $\pi/6$ (radian) for method II and III. The needle electrodes have radius 0.05 (cm) with distances $a_0 = 1$ (cm), $a = 1$ (cm), $b = 1$ (cm), $c = 0.5455$ (cm), $s = 0.9893$ (cm) (details in Fig. 1 b). To estimate the anisotropic permittivity of the domain, a sinusoidal current of 1 (mA) was injected from 1 kHz to 1 MHz. Experimental results verifying ‘Convergence’, ‘Sensitivity’ and ‘Robustness’ were performed at 1 kHz. The used transverse electrical conductivity σ_T is from 0.341 to 0.503 (S/m) and relative permittivity $\epsilon_{r,T}$ is from $2.59 \cdot 10^4$ to $1.84 \cdot 10^3$ (dimensionless) from skeletal muscle at specified frequencies^{35,36}. Longitudinal (denoted by the subscript L) permittivity values were computed from transverse permittivity values using a (constant) anisotropy ratio $\alpha^2 = 0.4$, unless otherwise noted. Methods I and II use needle impedance values Z_1 and Z_6 while method III uses Z_1, Z_6, Z_1^\perp , and Z_6^\perp . Simulated impedances in method I are obtained assuming $\phi = 0$, whereas method II and III assume $\phi = \pi/6$. Here, the angle $\phi = \pi/6$ for method II and III is chosen to satisfy the assumptions of the methods which is $\phi \neq 0$. Note that, in method II and III, ϕ may select any angle satisfying $\phi \neq 0$, which is the assumption of the method II and III. For the iteration process, the initial anisotropy ratio α^2 is set to 1 and consequently initial $K(\alpha^2, \phi)$ is obtained with $\alpha^2 = 1$.

Results

Numerical experiments were performed to evaluate three iterative reconstruction methods: (i), method I (corresponding equations are 17 - 21); (ii), method II (corresponding equations are 22, 23); (iii), method III (corresponding equations are 24, 25). The results confirm the convergence of the methods, their sensitivity to the presence of measurement noise, and their robustness to experimental positioning errors through numerical experiments. In addition, the three proposed methods were applied to estimate the electrical properties of the muscle, conductivity and relative permittivity, in the frequency range of 10 kHz to 1 MHz. The cross-shaped needle in method I has its major axis aligned with respect to the z -axis and the [ES] face is the yz -plane, i.e. $\theta = 0, \phi = 0, \varphi = 0$ (Fig. 2). Method I is then extended to method II by considering needle’s rotation angle $\phi \neq 0$. In this numerical simulation, we assume $\phi = \pi/6$ with respect to its major axis. For method III, the angle ϕ is assumed to be unknown. The two impedances z_1 and z_6 are used in both method I and method II. In method III, four impedances z_1, z_1^\perp, z_6 and z_6^\perp are used to estimate muscle permittivity values.

To compare the three methods, the following three observations were made; (1) ‘Convergence’: result error according to the number of iterations to which the method is applied (Fig. 8a), (2) ‘sensitivity’: result error according to the noise level (Fig. 8b), (3) ‘Robustness’: result error according to angle error (Fig. 8c). Method I was developed to be applied when the needle is inserted perpendicular to the muscle and one side of the needle is parallel to the direction of the muscle fiber. According to the experimental results, we recommend to use method I to obtain stable results at all SNRs, but to obtain accurate results, the angular misalignment with respect to the anisotropy direction should be less than 10 degrees. Method II was developed to be applied when the needle is inserted perpendicularly to the muscle, and the angle between one side of the needle, the direction of the muscle fiber is not 0 and the angle is known. According to the experimental results, method II should be used only when an SNR of 40 dB or more and a very accurate angular mismatch are guaranteed. Method III was developed to be

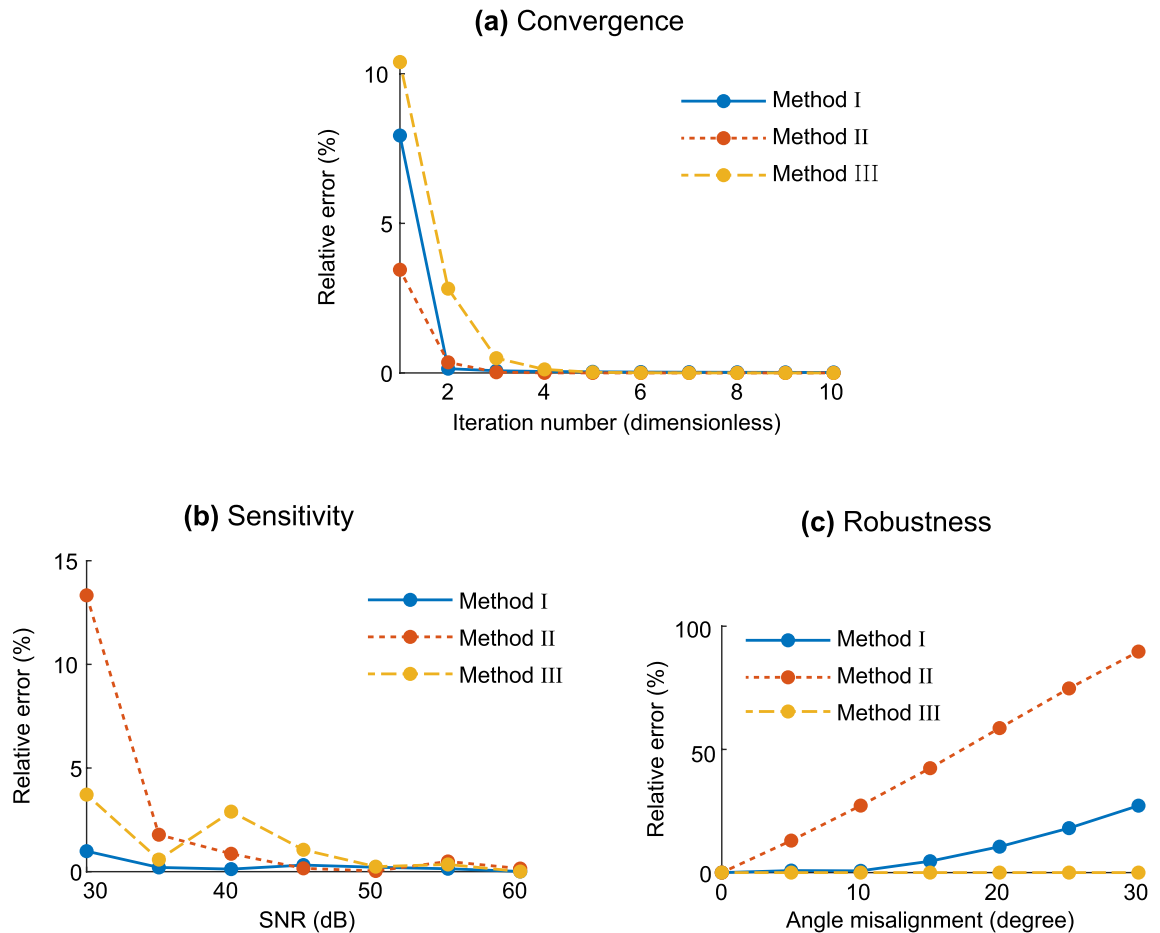


Figure 8. Performance comparison between methods considering the estimated anisotropy ratio α^2 . **(a)** Convergence of the with iteration number. **(b)** Sensitivity to measurement noise. **(c)** Robustness in front of needle angle misalignments.

applied when the needle is inserted perpendicular to the muscle. It can be applied without knowledge of muscle fiber orientation. Experimental results show that method III provides the most stable and accurate results when an SNR of 50 dB or higher is guaranteed.

Convergence. As mentioned above, the methods presented are iterative. Therefore, here we evaluate their convergence to the true permittivity value. We quantified the error of the resistivity anisotropy ratio α^2 as a function of the iteration number. Figure 8a shows all three methods proposed converge to the true value and the relative error is lower than 0.1% after five iterations. All three methods showed good convergence in which the error decreased as the number of iteration increased in common. If the number of iteration was less than 5 times, method II was the most accurate and method III was the least accurate, but if the number of repetitions was more than 5 times, all three methods had a very small error of close to 0%.

Sensitivity. Figure 8b shows the error of the estimated anisotropy ratio α^2 under the presence of random noise varying the SNR from 30 to 60 dB. Overall, these results show the estimated parameter is not sensitive to noise if the SNR is larger than 35 dB, with a relative error lower than 5%. The SNR is computed as

$$\text{SNR} = 10 \log_{10} \left(\frac{\text{impedance value}}{\text{standard deviation}} \right)^2 \quad (36)$$

From the given SNR range (30 to 60 dB), the simulated noisy impedance is generated with additive random noise sampled from standard Gaussian distribution with appropriate standard deviation. Methods I and III clearly showed a tendency for errors to decrease as SNR increased. Method II showed that as the SNR increased as a whole, the error tended to decrease, but when the SNR was 40–45 dB, an unexpected large error occurs. Since the measurement noise is randomly made, a large error may occur in the 40–45 dB SNR by chance. As a result of performing a number of random measurement noise at 30–60 dB, errors tend to decrease as SNR increases overall, but errors are large even in certain SNRs.

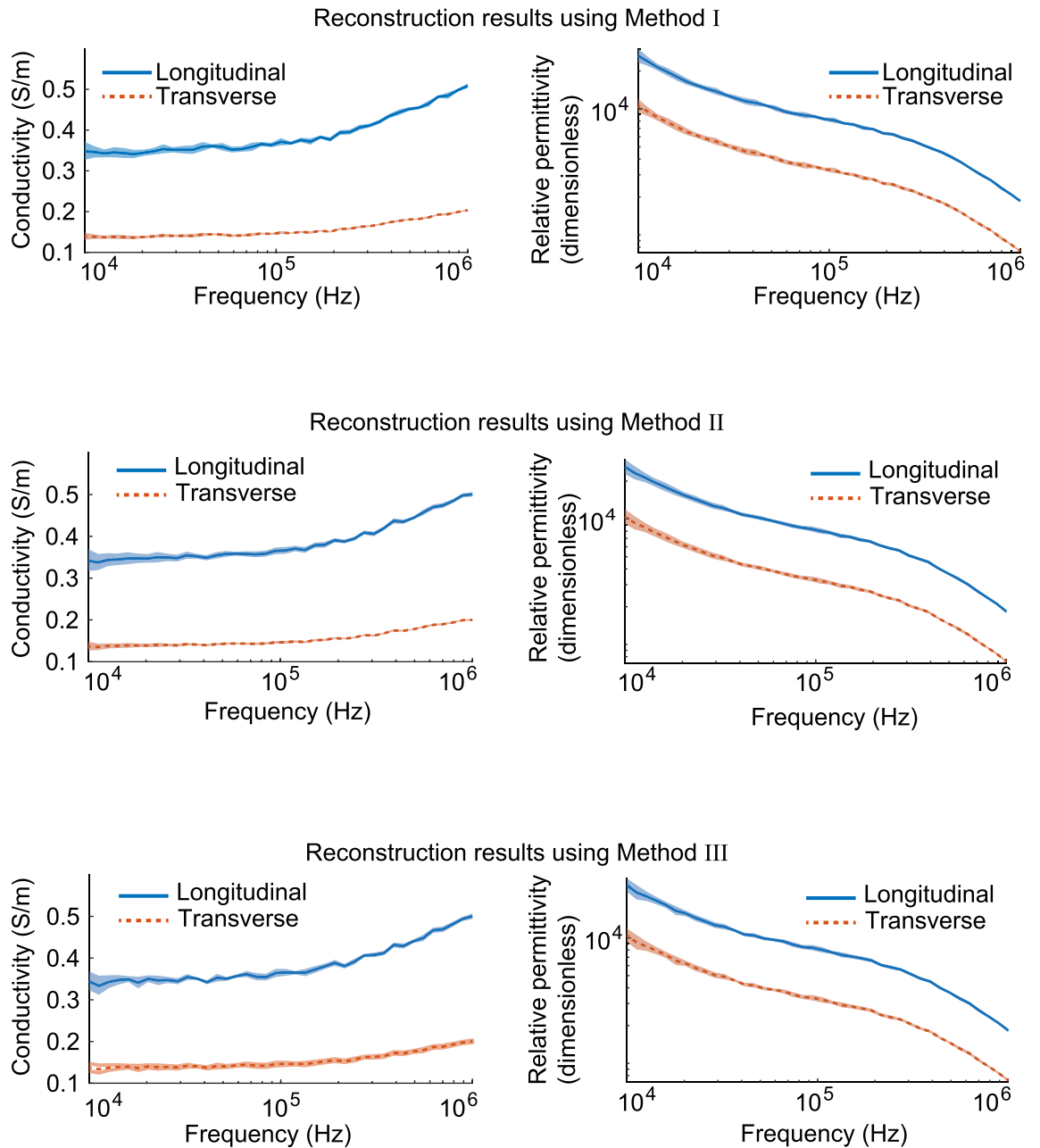


Figure 9. Estimated anisotropic permittivity (i.e., conductivity and relative permittivity) using method I, II, and III. The solid lines represent the true values, whereas the shaded area represent ± 3 times the standard deviation based on the estimated value.

Robustness. Figure 8c shows the reconstruction error of the estimated anisotropy ratio α^2 assuming an experimental misalignment of the cross-shaped needle once inserted into the muscle. Out of the three methods developed and tested, method III is the most robust to angle errors. Methods I and II are very weak against angle misalignment, in other words, the larger the angle mismatch, the greater the error. Method II is more vulnerable to angle misalignment than method I. On the other hand, method III is robust against angle misalignment, because it does not require any prior information about the angle. In this experiment, an error of less than 0.1% was shown in the case of angular misalignment.

Reconstruction of anisotropic muscle electrical properties. Figure 9 shows the results of estimating the conductivity and relative permittivity (electrical properties) of anisotropic muscles for frequencies using each of the three methods; method I (Eq. 18), (Eq. 21) with Z_1 and Z_6 , method II (23), (Eq. 24) with Z_1 and Z_6 , and method III (Eq. 29), (Eq. 30) with Z_1 , Z_1^\perp , Z_6 and Z_6^\perp . In this numerical experiment, when the angle misalignment was 1 degree and the noise SNR was 30 dB, the average and standard deviation of the estimated values were used by applying each method 10 times. The solid and dotted lines show true muscle electrical properties

(EP)^{35,36} and transparent areas represent ± 3 times the standard deviation (99.7% confidence interval) based on the estimated value from method I, II, and III. For all three methods, the true values were within the 99.7% confidence interval. The 99.7% confidence intervals for longitudinal and transverse EPs were small enough to distinguish between longitudinal and transverse EPs.

Discussion

This modeling study demonstrates the potential for using a novel cross-shaped needle for the assessment of two-dimensional anisotropic muscle permittivity property. While the technology itself still requires actual development, its potential for simplifying assessment of this electrical tissue property could be valuable. Specifically, by better understanding tissue permittivity, it could become possible to more accurately assess and understand alterations in muscle tissue in certain diseases and their impact on standard electrophysiological testing²⁵. For example, by applying this needle and analyzing the resulting data, it would become possible to better understand the origins of the morphology of motor unit potentials recorded at a distance from the source generator (i.e., the cumulative depolarizing myofiber membranes)²⁶. Similarly, we would be able to better understand the limits of detection of smaller discharges, such as fibrillation potentials, as one moves farther from the source. Indeed, these very basic concepts have been minimally studied to date and, in these authors' view, remain relatively poorly understood⁶. Detailed work in this area could greatly expand the basic tenets underlying the field of clinical neurophysiology.

Beyond these new insights into the underpinnings of acquired needle EMG data, the ability to measure tissue permittivity with a single needle could also have important direct clinical value^{27,28}. To date, needle impedance-related works require multiple simultaneous 4-electrode needle insertions to measure tissue permittivity^{20,21}. The invasiveness of these approaches limit their clinical translation, but this could be obviated with the construction and implementation of the needle design proposed here²⁹. Being able to measure the permittivity directly with a single needle insertion could open up an entirely new area of research with direct clinical application, including using these actual tissue property to assist in neuromuscular diagnosis, and even more importantly, to assess subtle effects of therapeutic intervention on muscle health.

There are several limitations to this study and our proposed needle design. First, this is only a modeling study and a number of both theoretical and practical simplifications have been made, including the assumption of relative homogeneity of muscle tissue. However, many NMDs are patchy with some regions of a given muscle being severely affected while other regions are entirely normal or only minimally affected^{30,31}. While we have made first inroads into modeling such heterogeneities³², this would have made our analysis here difficult and was not attempted here. Second, muscle conditions are not static and thus, it is possible that there may be changes in tissue permittivity making it difficult to align EMG data obtained even if there is a relatively short time lag between application of the cross-needle and the insertion of a standard concentric EMG needle in the same region. The third related concern is that this cross-needle itself might injure the muscle thus potentially altering impedance readings. Standard EMG needles are round for many reasons, a major one of which is to ensure patient comfort (as well, as of course, simplicity in design and manufacture). The needle designed here, although pointed, to some extent represents two orthogonal blades being inserted into the muscle. Even if relatively small, it would like still injure muscle and cause localized bleeding which in itself could negatively impact and distort the measured permittivity. It is worthwhile to note, however, that other large needles do exist and are used routinely for muscle assessment such as the Bergstrom biopsy needle, which actually typically requires a small incision in the overlying skin to place appropriately in the muscle. Of course, it may be theoretically possible to make this cross-needle very small (e.g., approximately 26 gauge, based on a circle circumscribing the cross), and thus keeping any tissue damage quite limited. A fourth concern is that, while we have included anisotropy in our analyses, as well as a study of needle misalignment, muscle fiber orientation can be complex, and thus this modeling remains a vast simplification of any observed data. Finally, muscle is a dynamic organ and in these analyses we have considered only the muscle at rest. However, in order to generate actual contraction of the muscle, motor unit potentials is required. Even an isometric contraction would still likely alter many aspects of muscle structure, including producing slight shifts in muscle fiber orientation (and hence anisotropy), altering the relative extracellular/intracellular volume ratios, and impacting muscle blood volume, a feature that was not even included in this model.

A single surface flat electrode can only be used in Methods I and II. In order to apply Method III, it is required to have a surface and its perpendicular surface. Accordingly, the minimum requirement is L-shaped needle electrode which has two planes perpendicular to each other. However, the reason why we proposed a cross-shaped needle electrode rather than an L-shaped needle electrode is because of (1) structural stability resulting from the symmetry of the shape, and (2) the efficiency of measuring four regions with one insertion.

In conclusion, we have performed a modeling study on a novel impedance-measuring needle that has the potential of providing robust assessments of muscle volume conduction properties. To move these innovative concepts forward, it will next be necessary to design and produce a working version of this needle electrode, likely for initial application and study in larger NMD animal models. This work is now being planned.

Received: 10 January 2022; Accepted: 9 May 2022

Published online: 19 May 2022

References

1. Destexhe, A. Spike-and-wave oscillations based on the properties of GABAB receptors. *J. Neurosci.* **18**, 9099–111 (1998).
2. Bédard, C., Kröger, H. & Destexhe, A. Modeling extracellular field potentials and the frequency-filtering properties of extracellular space. *Biophys. J.* **86**, 1829–1842 (2004).
3. Basser, P. J. & Roth, B. J. New currents in electrical stimulation of excitable tissues. *Annu. Rev. Biomed. Eng.* **2**, 377–397 (2000).

4. Coley, W. D. *et al.* Effect of genetic background on the dystrophic phenotype in mdx mice. *Hum. Mol. Genet.* **25**, 130–145 (2016).
5. van Putten, M. *et al.* Natural disease history of the D2 -mdx mouse model for Duchenne muscular dystrophy. *FASEB J.* (2019).
6. Luo, X., Wang, S., Rutkove, S. B. & Sanchez, B. Nonhomogeneous volume conduction effects affecting needle electromyography: An analytical and simulation study. *Physiol. Meas.* **42**, 115005 (2021).
7. Zhang, Xiaotong, Liu, Jiaen & He, Bin. Magnetic-resonance-based electrical properties tomography: A review. *IEEE Rev. Biomed. Eng.* **7**, 87–96 (2014).
8. Joyce, N. C., Oskarsson, B. & Jin, L.-W. Muscle biopsy evaluation in neuromuscular disorders. *Phys. Med. Rehabil. Clin. N. Am.* **23**, 609–631 (2012).
9. Wilbourn, A. J. The electrodiagnostic examination with myopathies. *J. Clin. Neurophysiol.* **10**, 132–48 (1993).
10. Nagy, J. A., DiDonato, C. J., Rutkove, S. B. & Sanchez, B. Permittivity of ex vivo healthy and diseased murine skeletal muscle from 10 kHz to 1 MHz. *Nat. Sci. Data* **6**, 37 (2019).
11. Prayson, R. A. Diagnostic yield associated with multiple simultaneous skeletal muscle biopsies. *Am. J. Clin. Pathol.* **126**, 843–848 (2006).
12. Dengler, J. *et al.* Differences in pain perception during open muscle biopsy and Bergstroem needle muscle biopsy. *J. Pain Res.* **7**, 645–650 (2014).
13. Schwan, H. & Kay, C. Specific resistance of body tissues. *Circ. Res.* **4**, 664–670 (1956).
14. Geddes, L. A. & Baker, L. E. The specific resistance of biological material-A compendium of data for the biomedical engineer and physiologist. *Med. Biol. Eng.* **5**, 271–293 (1967).
15. Stoy, R. D., Foster, K. R. & Schwan, H. P. Dielectric properties of mammalian tissues from 0.1 to 100 MHz; A summary of recent data. *Phys. Med. Biol.* **27**, 501–513 (1982).
16. Pethig, R. Dielectric properties of body tissues. *Clin. Phys. Physiol. Meas.* **8**(Suppl A), 5–12 (1987).
17. Surowiec, A., Stuchly, S. S. & Swarup, A. Postmortem changes of the dielectric properties of bovine brain tissues at low radiofrequencies. *Bioelectromagnetics* **7**, 31–43 (1986).
18. Schaefer, M., Gross, W., Ackemann, J. & Gebhard, M. M. The complex dielectric spectrum of heart tissue during ischemia. *Bioelectrochemistry (Amsterdam, Netherlands)* **58**, 171–80 (2002).
19. Rossmanna, C. & Haemmerich, D. Review of temperature dependence of thermal properties, dielectric properties, and perfusion of biological tissues at hyperthermic and ablation temperatures. *Crit. Rev. Biomed. Eng.* **42**, 467–92 (2014).
20. Kwon, H., Nagy, J. A., Taylor, R., Rutkove, S. B. & Sanchez, B. New electrical impedance methods for the in situ measurement of the complex permittivity of anisotropic biological tissues. *Phys. Med. Biol.* **62**, 8616–8633 (2017).
21. Kwon, H., Guasch, M., Nagy, J. A., Rutkove, S. B. & Sanchez, B. New electrical impedance methods for the in situ measurement of the complex permittivity of anisotropic skeletal muscle using multipolar needles. *Sci. Rep.* **9**, 3145 (2019).
22. Kwon, H., Rutkove, S. B. & Sanchez, B. Recording characteristics of electrical impedance myography needle electrodes. *Physiol. Meas.* **38**, 1748–1765 (2017).
23. Kwon, H., Di Cristina, J. F., Rutkove, S. B. & Sanchez, B. Recording characteristics of electrical impedance-electromyography needle electrodes. *Physiol. Meas.* **39**, 055005 (2018).
24. Cardoner, MMd. M. *et al.* Modeling and reproducibility of twin concentric electrical impedance myography. *IEEE Trans. Biomed. Eng.* **68**, 3068–3077 (2021).
25. Sanchez, B., Martinsen, O. G., Freeborn, T. J. & Furse, C. M. Electrical impedance myography: A critical review and outlook. *Clin. Neurophysiol.* **132**, 338–344 (2021).
26. Luo, X., Wang, S. & Sanchez, B. Modeling and simulation of needle electrical impedance myography in nonhomogeneous isotropic skeletal muscle. *IEEE J. Electromagn. RF Microwaves Med. Biol.* (2021) (in press).
27. Rutkove, S. B., Kwon, H., Guasch, M., Wu, J. S. & Sanchez, B. Electrical impedance imaging of human muscle at the microscopic scale: A multi-electrode needle device: A simulation study. *Clin. Neurophysiol.* **129**, 1704–1708 (2018).
28. Sanchez, B. & Rutkove, S. B. Electrical impedance myography and its applications in neuromuscular disorders. *Neurotherapeutics* **14**, 107–118 (2017).
29. Rutkove, S. B., Le, M., Ruehr, S. A., Nagy, J. A., Semple, C. & Sanchez, B. Design and pilot testing of a 26-gauge impedance-electromyography needle in wild-type and ALS mice. *Muscle Nerve* **1–7** (2022).
30. Hamel, J. *et al.* Magnetic resonance imaging correlates with electrical impedance myography in facioscapulohumeral muscular dystrophy. *Muscle & Nerve* **61**, 644–649 (2020).
31. Wattjes, M. P., Kley, R. A. & Fischer, D. Neuromuscular imaging in inherited muscle diseases. *Eur. Radiol.* **20**, 2447–2460 (2010).
32. Luo, X., Wang, S. & Sanchez, B. A framework for modeling bioimpedance measurements of nonhomogeneous tissues: A theoretical and simulation study. *Physiol. Meas.* **42**, 055007 (2021).
33. Plonsey, R. & Heppner, D. B. Considerations of quasi-stationarity in electrophysiological systems. *Bull. Math. Biophys.* **29**, 657–664 (1967).
34. Rush, S. Methods of measuring the resistivities of anisotropic conducting media in situ. *J. Res. Natl. Bureau Standards Sect. C Eng. Instrum.* **66C**, 217 (1962).
35. Andreuccetti, D., Fossi, R. & Petrucci, C. An Internet resource for the calculation of the dielectric properties of body tissues in the frequency range 10 Hz–100 GHz. Based on data published by C. Gabriel *et al.* in 1996. [Online]. <http://niremf.ifac.cnr.it/tissprop/> (1997).
36. Gabriel, C., Gabriel, S. & Corthout, E. The dielectric properties of biological tissues: I. Literature survey. *Phys. Med. Biol.* **41**, 2231–49 (1996).

Acknowledgements

This research was supported by grant NIH/NINDS R41 RNS112029A (BS) and NRF/MSIT 2020R1F1A1A0107244511 (HK,HCP).

Author contributions

Developed the methods: H.K. and B.S. Conceived and designed the experiments: H.K. and B.S. Performed the experiments: H.C.P. and A.C.B. Analyzed the data: H.K. and B.S. Wrote the paper: H.K., S.R. and B.S. All authors revised and approved the manuscript.

Competing interests

Dr. Sanchez holds equity in Haystack Diagnostics, a company that develops clinical needle impedance technology for neuromuscular evaluation. The company has an option to license patented needle impedance technology where the author is named an inventor. He also holds equity and serves as Scientific Advisory Board Member of Ioniq Sciences, a company that develops clinical impedance technology for early cancer detection. Dr. Sanchez serves as Scientific Advisor to the Board of B-Secur, a company that develops wearable ECG and impedance technology, he also holds equity of the company. He consults for Myolex, Inc., a company that develops surface

impedance technology. The company has an option to license patented surface EIM technology where the author is named an inventor. Dr. Sanchez also serves as a consultant to Impedimed, Texas Instruments, Happy Health, Maxim Integrated, and EKO Health companies that develop impedance related technology for consumer use. This study did not employ any relevant company technology.

Additional information

Correspondence and requests for materials should be addressed to H.K. or B.S.

Reprints and permissions information is available at www.nature.com/reprints.

Publisher's note Springer Nature remains neutral with regard to jurisdictional claims in published maps and institutional affiliations.



Open Access This article is licensed under a Creative Commons Attribution 4.0 International License, which permits use, sharing, adaptation, distribution and reproduction in any medium or format, as long as you give appropriate credit to the original author(s) and the source, provide a link to the Creative Commons licence, and indicate if changes were made. The images or other third party material in this article are included in the article's Creative Commons licence, unless indicated otherwise in a credit line to the material. If material is not included in the article's Creative Commons licence and your intended use is not permitted by statutory regulation or exceeds the permitted use, you will need to obtain permission directly from the copyright holder. To view a copy of this licence, visit <http://creativecommons.org/licenses/by/4.0/>.

© The Author(s) 2022